

- Kutsch, J. *Comp. Physiol. A Sens. Neural Behav. Physiol.* **161**, 115 (1987); D. E. Claassen and A. E. Kammer, *J. Neurobiol.* **17**, 1 (1986).
23. R. Menzel, *Naturwissenschaften* **70**, 504 (1983); R. H. Scheller *et al.*, *Cell* **32**, 7 (1983); J. W. Truman and L. M. Schwartz, *J. Neurosci.* **4**, 274 (1984); N. J. Tublitz, P. F. Copenhauer, P. H. Taghert, J. W. Truman, *Trends Neurosci.* **9**, 359 (1986).
 24. B. S. Beltz and E. A. Kravitz, *J. Neurosci.* **3**, 585 (1983).
 25. D. R. Nassel, *Prog. Neurobiol.* **30**, 1 (1988); A. M. Valles and K. White, *J. Neurosci.* **6**, 1482 (1986); *J. Comp. Neurol.*, in press; V. Budnik and K. White, *ibid.*, in press.
 26. P. H. Taghert and C. S. Goodman, *J. Neurosci.* **4**, 989 (1984); D. K. Stuart, S. S. Blair, D. A. Weisblat, *ibid.* **7**, 1107 (1987).
 27. D. A. Steindler, *Brain Res.* **223**, 367 (1981).
 28. M. S. Livingstone, R. M. Harris-Warrick, E. A. Kravitz, *Science* **208**, 76 (1980).
 29. R. Kawagoe, K. Onodera, A. Takeuchi, *J. Physiol. (London)* **312**, 225 (1981).
 30. M. Otsuka *et al.*, *Proc. Natl. Acad. Sci. U.S.A.* **56**, 1110 (1966).
 31. S. Glusman and E. A. Kravitz, *J. Physiol. (London)* **325**, 223 (1982).
 32. H. Grundfest and J. P. Reuben, in *Nervous Inhibition*, E. Florey, Ed. (Pergamon, Oxford, 1961), pp. 92–104; J. Dudel, *Naunyn-Schmiedeberg's Arch. Exp. Pathol. Pharmacol.* **249**, 515 (1965); L. Fischer and E. Florey, *J. Exp. Biol.* **102**, 187 (1983).
 33. C. A. Breen and H. L. Atwood, *Nature* **303**, 716 (1983).
 34. R. M. Harris-Warrick and E. A. Kravitz, *J. Neurosci.* **4**, 1300 (1984).
 35. C. A. G. Wiersma and K. Ikeda, *Comp. Biochem. Physiol.* **12**, 509 (1964); W. H. Evoy and D. Kennedy, *J. Exp. Zool.* **165**, 223 (1967).
 36. M. S. Livingstone, S. F. Schaeffer, E. A. Kravitz, *J. Neurobiol.* **12**, 27 (1981).
 37. B. S. Beltz and E. A. Kravitz, *J. Neurosci.* **7**, 533 (1987).
 38. E. A. Kravitz *et al.*, in *Model Neural Networks and Behavior*, A. I. Selverston, Ed. (Plenum, New York, 1985), pp. 339–360.
 39. K. K. Siwicki, B. S. Beltz, E. A. Kravitz, *J. Neurosci.* **7**, 522 (1987).
 40. P. Ma, B. S. Beltz, E. A. Kravitz, unpublished observations.
 41. B. S. Beltz, M. Pontes, E. A. Kravitz, unpublished observations.
 42. J. C. E. Scrivener, *Fish. Res. Board Can. Tech. Rep.* **235**, 1 (1971); J. Atema and J. S. Cobb, in *The Biology and Management of Lobsters*, J. S. Cobb and B. F. Phillips, Eds. (Academic Press, New York, 1980), pp. 409–450.
 43. V. M. Pasztor and B. M. H. Bush, *Nature* **326**, 793 (1987).
 44. P. G. Montarolo *et al.*, *Science* **234**, 1249 (1986); N. Dale, E. R. Kandel, S. Schacher, *J. Neurosci.* **7**, 2232 (1987); D. B. Pritchett and J. L. Roberts, *Proc. Natl. Acad. Sci. U.S.A.* **84**, 5545 (1987); S. J. Yeung and A. Eskin, *ibid.*, p. 279.
 45. E. V. Jensen *et al.*, *Proc. Natl. Acad. Sci. U.S.A.* **59**, 632 (1968).
 46. M. E. Greenberg, E. B. Ziff, L. A. Greene, *Science* **234**, 80 (1986); F. W. George and S. R. Ojeda, *Proc. Natl. Acad. Sci. U.S.A.* **84**, 5803 (1987); J. I. Morgan, D. R. Cohen, J. L. Hempstead, T. Curran, *Science* **237**, 192 (1987).
 47. R. M. Harris-Warrick and R. E. Flamm, *Trends Neurosci.* **9**, 432 (1986).
 48. Supported by NIH grants NS-07848 and NS-25915 and funds from Harvard Medical School. Special thanks for reading this manuscript to J. Hildebrand, E. Arbas, L. Regan, P. Ma, and L. Geller, and for technical help to D. Cox and J. Gagliardi. The ideas expressed in this article derive from interactions with many outstanding collaborators over the years. The article was written in the library of the Marine Biological Laboratory in Woods Hole, MA. I thank the staff of that library and L. Thimas for their help and support.

Research Articles

Soft X-ray Images of the Solar Corona with a Normal-Incidence Cassegrain Multilayer Telescope

ARTHUR B. C. WALKER, JR., TROY W. BARBEE, JR., RICHARD B. HOOVER,
JOAKIM F. LINDBLOM

High-resolution images of the sun in the soft x-ray to extreme ultraviolet (EUV) regime have been obtained with normal-incidence Cassegrain multilayer telescopes operated from a sounding rocket in space. The inherent energy-selective property of multilayer-coated optics allowed distinct groups of emission lines to be isolated in the solar corona and the transition region. The Cassegrain telescopes provided images in bands centered at 173 and 256 angstroms. The bandpass centered at 173 angstroms is dominated by emission from the ions Fe IX and Fe X. This emission is from coronal plasma in the temperature range 0.8×10^6 to 1.4×10^6 K. The images have angular resolution of about 1.0 to 1.5 arc seconds, and show no degradation because of x-ray scattering. Many features of coronal structure, including magnetically confined loops of hot plasma, coronal plumes, polar coronal holes, faint structures on the size scale of supergranulation and smaller, and features due to overlying cool prominences are visible in the images. The density structure of polar plumes, which are thought to contribute to the solar wind, has been derived from the observations out to 1.7 solar radii.

THE STUDY OF THE SOLAR ATMOSPHERE IS COMPLICATED IN that the sizes of the fundamental structures that control the important physical processes are below the resolution limit possible with instruments now available for all wavelengths. This problem is a consequence generally of the dominant influence of the solar magnetic field, which is characterized by structure on the scale of 70 kilometers (0.1 arc second as viewed from Earth) or less (1). The problem has been especially acute for soft x-ray observations because the available techniques could not provide observations with both high spatial and high spectral resolution simultaneously.

Most solar x-ray observations have been made with grazing-incidence optical systems (2). These systems, which were first developed 40 years ago (3, 4), have been used successfully to observe the solar corona (5) and to study cosmic x-ray sources (6). Grazing-incidence optics can provide high-quality images, but they have no inherent ability to resolve spectral features. Consequently, images obtained with grazing-incidence optics and thin filters are of low to moderate spectral resolution, and they cannot be used to isolate

A. B. C. Walker, Jr., and J. F. Lindblom are at the Center for Space Science and Astrophysics, Stanford University, Stanford, CA 94305. T. W. Barbée, Jr., is at Lawrence Livermore National Laboratory, Livermore, CA 94550. R. B. Hoover is at the Space Science Laboratory, National Aeronautics and Space Administration, Marshall Space Flight Center, Huntsville, AL 35812.

material at a single temperature or to resolve macroscopic dynamical effects (which require the study of line profiles). Observations with dispersive spectrometers (7, 8) can provide high spectral resolution, but resolution of the physical structures responsible for the emission is limited.

Significant advances in the development of normal-incidence x-ray optics (9) now allow their use for solar observations. Normal-incidence x-ray telescopes have mirrors coated with multiple thin atomic layers ("multilayers"). These layered structures act as Bragg diffractors for soft x-ray and extreme ultraviolet (EUV) radiation (1 to 1000 Å). Multilayer structures, when deposited on substrates of sufficient smoothness and optical precision, can act as optical elements in scanning microscopes (10), spectroscopic instruments (11), and astronomical telescopes (12). Multilayer optics have already had a significant impact on laboratory studies of solids (13), biological systems (14), and plasmas (15).

We have used normal-incidence multilayer optics in a Cassegrain telescope to obtain images of the solar corona in the 171 to 175 Å bandpass. These high-resolution images were obtained from a Nike-Black Brant sounding rocket launched at 1805 universal time (UT) on 23 October 1987 from the White Sands Missile Range, New Mexico. Many coronal structures are visible in the images (Fig. 1, A and D). In this article, we compare these images with images obtained at other wavelengths to indicate how the structure of the solar plasma varies with temperature (Fig. 1, A, B, and C) and how the structure is shaped by solar magnetic fields (Fig. 1, E and F). The Cassegrain telescope images demonstrate that multilayer optics can furnish high-resolution images and spectroscopic analysis simultaneously, a capability that has only now become available to x-ray astronomers and solar physicists (16).

Multilayer x-ray-EUV optics. Grazing-incidence high-resolution x-ray telescopes and microscopes have been designed almost

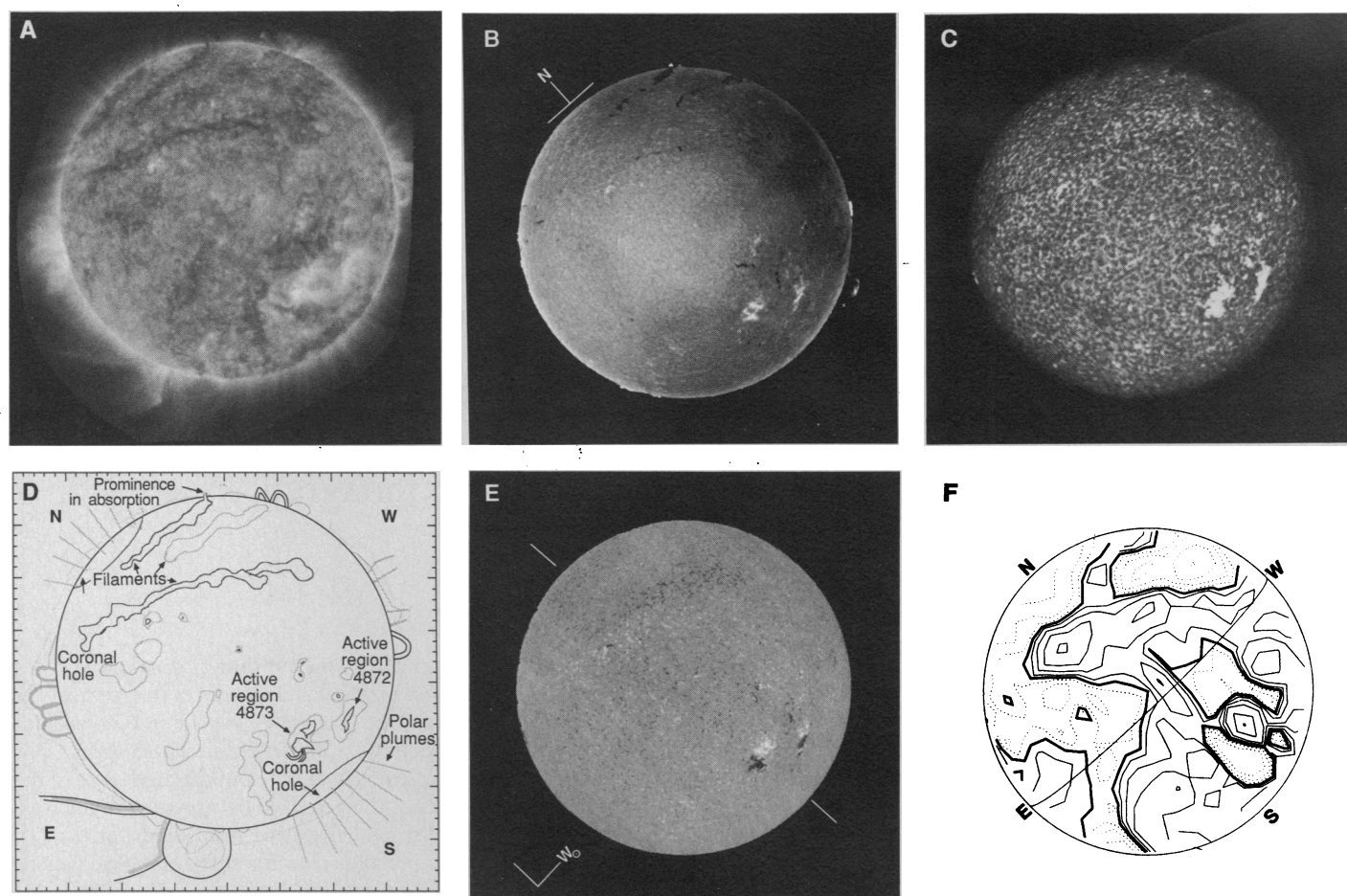


Fig. 1. (A) The solar corona as photographed in the emission of the resonance lines of Fe IX at 171 Å and Fe X at 174.5 Å, on 23 October 1987 at 1809 UT. The length of the exposure was 64 seconds. The dark bands visible at northern latitudes are due to overlying cool prominences, which are also clearly visible in (B). The image corresponds to coronal structures from approximately 0.8×10^6 to 1.4×10^6 K. (B) The sun as photographed in the light of the Balmer- α ($H\alpha$) absorption line of hydrogen at 6563 Å with a bandpass of 0.5 Å at 1510 UT on 23 October 1987. The core of the $H\alpha$ line is formed in the chromosphere in the temperature range 6000 to 7000 K. [Photograph courtesy of D. Speich, National Oceanic and Atmospheric Administration, Boulder, Colorado] (C) The solar chromosphere at 1579 UT on 23 October in the K_3 absorption line of Ca II ($\lambda = 3934$ Å). The photograph was made with a 0.3 Å wide filter. The Ca II K_3 line, which is formed at approximately 1×10^4 K, displays the structure of the chromospheric network (46). [Photograph courtesy of B. Labonte and D. Braun, University of Hawaii Mees Solar Observatory, Haleakala, Maui, Hawaii] (D) Locations of various phenomena in A. The fiducial marks are at

1-arc-minute intervals. (E) Kitt Peak magnetogram for 23 October (1725 UT) showing the fine structure of the solar magnetic field. The gray indicates neutral regions, black negative polarity, and white positive polarity. The active regions, seen in the 173 Å image where emission from the magnetically confined coronal plasma is most intense, are clearly associated with bipolar regions with strong magnetic fields. The resolution of the magnetogram is 1.0 arc second. [Photograph courtesy of Jack Harvey of the National Solar Observatory, Tucson, Arizona] (F) Stanford magnetogram for 24 October 1987 (2124 UT) showing the large-scale structure of the solar magnetic field. The dark lines indicate the location of the neutral lines. The solid contours indicate positive polarity, and the dashed contours indicate negative polarity. The resolution of the magnetogram, which is intended to portray large-scale magnetic structure, is 3 arc minutes. Because of inclement weather, no magnetogram was obtained on 23 October. [Photograph courtesy of Phil Scherrer, Stanford University Wilcox Solar Observatory, Stanford, California]

Fig. 3. Resolution of the multilayer Cassegrain telescope. The theoretical resolution curves were computed by Shealy *et al.* (32). The rise in measured visible light resolution at 17 arc minutes off-axis is due to diffraction effects caused by vignetting.

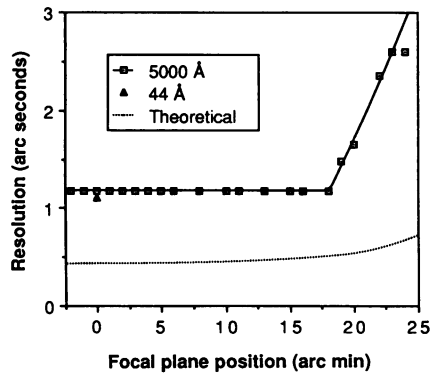
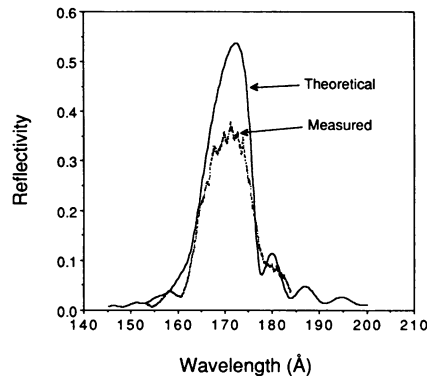


Fig. 4. Spectral response of a single multilayer mirror.



largely restricted to the 171 to 175 Å bandpass (Fig. 2) by the combination of the two reflections from the multilayer mirrors, and the L absorption edge of the aluminum filter. The resulting spectral resolving power, $\lambda/\Delta\lambda$, is about 40 (The location of the Al-L edge improved the resolving power of the telescope over that of the multilayer mirrors alone.) The images obtained with the 171 to 175 Å Cassegrain are dominated (86 percent) by the emission lines of Fe IX and Fe X which have maximum excitation from 0.8×10^6 to 1.4×10^6 K (Table 1) (29–31). The cooler O V and O VI lines contribute less than 6 percent of the solar flux in the telescope bandpass.

We measured the resolution of the Cassegrain telescope at both visible and in x-ray wavelengths (26, 32) (Fig. 3). Tests at 5000 Å demonstrated that the diffraction-limited resolution (defined as the ability to resolve two adjacent point sources on Kodak high-resolution photographic plates) was 1.2 arc seconds. Because well-collimated beams of 173 or 256 Å radiation with the appropriate diameter were not available, we measured the x-ray resolution of the Cassegrain with 44.7 Å radiation, available in the 300-meter-long MSFC x-ray test and calibration facility. We manufactured a special set of Cassegrain optics with a tungsten-carbon multilayer having the appropriate d -spacing (22.45 Å) for these tests. The measured resolution at 44.7 Å was 1.1 arc seconds.

We fabricated the multilayer mirrors, using previously described techniques (33). The multilayers on the mirrors in the 171 to 175 Å telescope are molybdenum-silicon pairs with the spacing 36.8 Å and 55.2 Å. The effective layer-pair spacing d_{eff} at $\lambda = 171$ Å is about 85.5 Å; this spacing is less than the sum of the physical thicknesses of each thin film because of refraction effects. Molybdenum-silicon was chosen because of its high reflectivity above the silicon L edge ($\lambda > 123$ Å), moderate spectral resolution ($\lambda/\Delta\lambda \sim 15$ for a single reflection and ~ 25 for two reflections) at 171 Å and excellent long-term stability (34). The effective $2d$ spacing and the mirror reflectivity were measured with a laser-generated plasma source and grating spectrometer (35). We were able to compare the measured and theoretical spectral responses (Fig. 4). The measured peak reflectiv-

ity of 0.35 was 66 percent of the predicted peak reflectivity of 0.53 (36). The super-polished spherical substrates used (37) had a surface smoothness near 3 Å rms as judged by measurements on similar substrates (38).

The images were recorded on an EUV-sensitive, tabular grain (T-grain) (39) emulsion that was specially prepared for us by the Eastman Kodak Company. This emulsion is similar to Kodak TMAX 100, but was prepared without a gelatin overcoat for optimum performance in the EUV. The 35-mm film had a Rem-Jet backing which prevented static discharges during film transport in the vacuum; the film was transported in conventional Canon T-70 cameras with no adverse effects. Previous observations in the EUV region have been carried out with Schumann emulsions (40), which are extremely sensitive to contaminants and abrasions and yield a maximum photographic diffuse density no greater than 1.6. Our T-grain emulsion yielded densities greater than 3.0 (semispecular densities greater than 3.9), and the T-grain 100 film provided high sensitivity throughout the spectral region studied during this flight (8 to 256 Å). The film obtained from the 171 to 175 Å Cassegrain was processed to yield a visible light ASA (American Standards Association) speed equivalent of 400, thus providing optimum sensitivity to faint features in the far corona. Hoover *et al.* (41) have discussed the advantages of these new T-grain films at soft x-ray–EUV wavelengths.

Observations. A wide range of coronal features are visible in the bandpass between 171 and 175 Å (Figs. 1A and 5). These images complement the information that can be obtained (i) from images in the spectral region from 1 to 30 Å (7), which is most effectively studied with grazing-incidence optical systems (42), and (ii) from the spectral region between 304 and about 600 Å, (43) which is accessible to conventional single-reflection optics (16, 44). Below 30 Å, emission of the nonflaring solar atmosphere is dominated by hot ($\geq 2.0 \times 10^6$ K), dense (about 10^8 ions per cubic centimeter) plasma confined in magnetic flux tubes (45). Between 304 Å and about 600 Å, solar emission is dominated by plasma from 2×10^5 K to 1×10^6 K [the transition region (46, 47)], which is strongly confined by the highly structured magnetic field of the chromospheric network (Fig. 1C).

Changes in the structure of the atmosphere occur between 1×10^6 K and 1.5×10^6 K. In closed-field regions much of the gas at these temperatures is confined in loop structures (45). Systems of coronal loops are visible on the limb in the northwest, west, and east (Figs. 1, A and D, and 5), and are responsible for the emission visible from active regions 4872 and 4873 (see also Fig. 1E), at south 60°, west 0° to 50°. In open-field regions, where the coronal plasma is expanding into the solar wind, structures such as streamers and polar plumes (47) that are at the interface between the corona and the interplanetary medium, are visible in the 171 to 175 Å images at 1×10^6 K to 1.5×10^6 K (Figs. 1, A and D, and 5). Streamers, representing the corona–solar wind interface, are visible virtually everywhere on the limb, including coronal plumes in the polar regions, which are otherwise deficient in emission. Coronal holes, representing regions that generally lack closed magnetic structures capable of confining hot plasma, are clearly visible at the poles.

Other features that are visible in the 171 to 175 Å images are regions of low emission that coincide with large-scale loops of cool gas embedded in the hotter coronal gas that produces the 171 to 175 Å emission. These loops of gas at chromospheric temperatures (6×10^3 K to 3×10^4 K typically) are called prominences (48), and can be observed in emission above the limb (Fig. 1, A and D). Prominences observed in absorption on the disk [for example, in the Balmer- α ($H\alpha$) line images at 6563 Å (Fig. 1B)] are called filaments. Spectacular examples of such structures have been ob-

served in He II Lyman- α line images at 304 Å (16). Some of the "prominence cavities" (or filaments) seen in our images are also clearly visible in the H α chromospheric image (Fig. 1B). A dark feature that crosses the northwest limb at 70° latitude (Fig. 1A) can be seen in emission above the limb in the H α image (Fig. 1B). Because they are cooler, prominences represent material that is considerably denser than the surrounding coronal gas. The cool gas is supported against gravity by the magnetic field, and hence prominences occur at locations where the field is horizontal (that is, where the vertical component of the field is zero). These "neutral lines," which are closely delineated on the large-scale magnetic field map (Fig. 1F), are well correlated with regions of low emission in the 171 to 175 Å images. Although the depressed emission at 171 to 175 Å associated with prominence cavities may be due in part to the

exclusion of hot gas from the vicinity of the neutral line, the abrupt decrease in emission at the northwest limb associated with the prominence at 70° latitude suggests that prominence gas is also absorbing 171 to 175 Å emission from hot material lying below or behind the prominence loop. Considerably more prominence structure is visible in the 171 to 175 Å images than in the H α image, possibly because some of the prominence material is at temperatures where all of the hydrogen is ionized, and unable to absorb H α radiation. The absorption we observe is occurring in the He II continuum, shortward of 227 Å. Schmahl *et al.* and Schmahl and Orrall (49) have commented on a similar phenomenon occurring in the H I continuum. The large absorption feature in the southeast of our images at 45° latitude on the limb is an example of this phenomenon, and may represent a giant helmet streamer (50).

Another feature of interest is the structure extending toward the northeast from a point on the southeast limb at 40° latitude. This structure could represent a coronal spray, material ejected from the region of a flare behind the limb in the low corona. (There is no record of a flare occurring on the visible side of the limb near the time of our observation.) Such structures have been observed in He II Lyman α images (16); our observations indicate that large sprays in radiation may also be observed from an ion present in plasma at 1×10^6 K.

The images of Figs. 1A and 5 reveal that the corona is very complex at 1×10^6 K, with cool material embedded in the hot corona. Among the structures more clearly resolved in our images compared to earlier images are coronal loops on various size scales, polar plumes in emission, and prominence cavities on the disk and above the limb. Fine structure that appears to be related to supergranulation can also be seen on the disk (Fig. 5). Further analyses should yield information on a number of critical problems of coronal structure, including the nature of the chromospheric network in the lower corona, the structure of the corona-solar wind interface, the nature of the prominence-corona interface, and the nature of coronal loops.

Polar plumes. Polar plumes are believed to be the major source of the high-speed solar wind streams associated with coronal holes. Withbroe (51) has reviewed models of polar plumes and pointed out the importance of high-resolution (~ 1 arc second) observations of polar plumes to an understanding of the physics of coronal holes. Previous observations of polar plumes (on Skylab) in the soft x-ray and EUV (52-54), have been limited in resolution to about 3 to 5

Table 1. Solar lines within the Cassegrain bandpass

Wave-length* (Å)	Intensity (I)† (10^{-3} ergs $\text{cm}^{-2} \text{sec}^{-1}$)	Tem- perature (10^6 K)	Ion	Contribution‡ (percentage)
167.495	2.5	0.80	Fe VIII	0.10
168.176	4.6	0.80	Fe VIII	0.20
168.548	2.	0.80	Fe VIII	0.10
168.933	1.6 ¹	0.80	Fe VIII	0.07
171.075	51.5	1.00	Fe IX	45.9
171.359	5.0§	2.50	Ni XIV	4.8
172.174	1.1	0.25	O V	1.1
172.936	1.4	0.30	O VI	1.3
173.081	3.0	0.30	O VI	2.9
174.534	52.7	1.25	Fe X	37.3
175.266	4.5	1.25	Fe X	2.1
175.474	1.3	1.25	Fe X	0.45
176.694	2.5	2.80	Ni XV	0.15
177.243	29.0	1.25	Fe X	0.70
178.060	2.0	1.55	Fe XI	0.04
179.762	1.0§	1.55	Fe XI	0.05
180.407	59.0	1.55	Fe XI	2.50
180.600	2.0	1.55	Fe XI	0.07
181.140	2.7	1.55	Fe XI	0.07
186.885	9.8	2.00	Fe XII	0.08
188.219	39.8	1.55	Fe XI	0.22

95.85

*From (36). †Measured by Malinovsky and Heroux (37) except for $\lambda=171.359$ and 179.762 Å. ‡ $\sum_i \epsilon_i \sum_j \epsilon_j$, where i and j are solar lines and the sum is over all the lines in the table; ϵ is taken from Fig. 4. §Estimated from the computations of Doschek and Cowan (38).

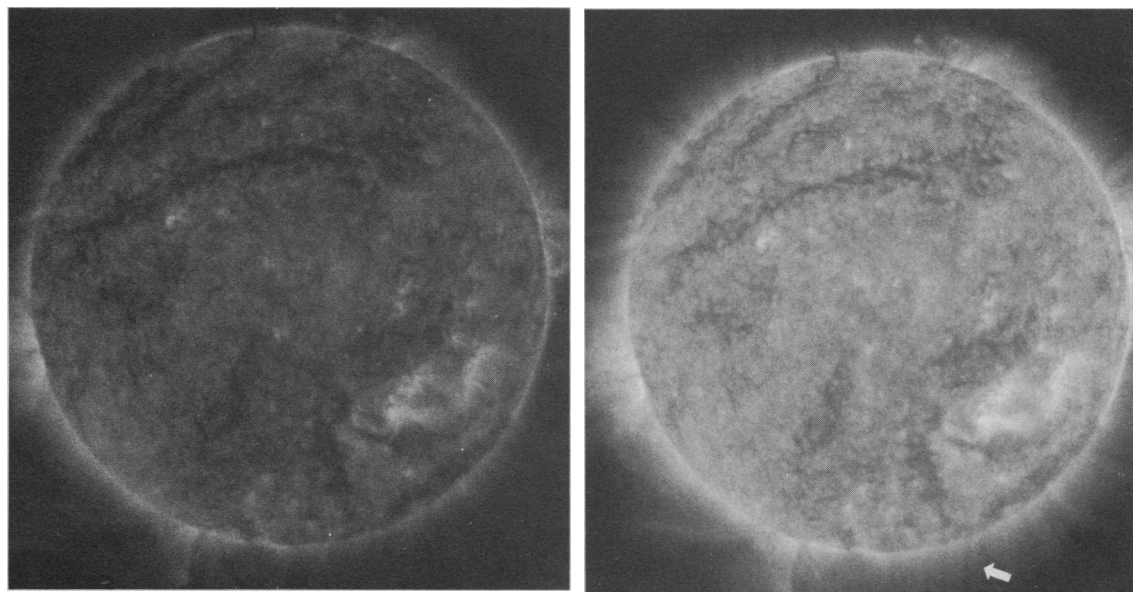
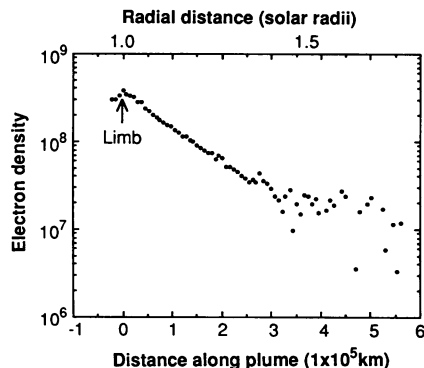


Fig. 5. The corona in the bandpass λ 171 to 175 Å as photographed with an 8-second exposure (left) and a 200-second exposure (right). The polar plume analyzed in Fig. 6 is indicated by the arrow.

Fig. 6. Density structure of a typical polar plume (the plume is marked with an arrow in Fig. 5). The electron density is plotted as a function of distance along the plume and as a function of radial distance from the center of the sun (the radius of the sun is 6.96×10^5 km). The scatter of the data points toward the low-density edge is due to grain noise in the film.



arc seconds, and to distances of 0.4 solar radii or less above the limb. To demonstrate the power of multilayer optics for the study of the structure of the interface between the corona and the solar wind, we examined the structure of a typical polar plume (Fig. 5). We calculated plume densities assuming that the plume is isothermal with a temperature of about 1.1×10^6 K, a value consistent with previous analysis of Skylab observations. The mean electron density ($\sqrt{\langle n_e^2 \rangle}$) in the plume in a resolution element ($\Delta x \Delta y$) can then be derived from the coronal excitation equation (7), which expresses the intensity in any emission line λ_{ij} as

$$I_{ij} = \frac{hc}{\lambda_{ij}} a_H A_Z \int_{\Delta x} dx \int_{\Delta y} dy \int_{-\infty}^{\infty} ds a_{Zz}(T_e) \alpha_{ji}(T_e) n_e^2$$

$$= \frac{hc}{\lambda_{ij}} \langle n_e^2 \rangle a_H A_Z \int_{\Delta x} dx \int_{\Delta y} dy \int_{-\infty}^{\infty} ds a_{Zz}(T_e) \alpha_{ji}(T_e)$$

where s is the coordinate along the line of sight. This equation is based on the assumption that the observed emission is due entirely to collisional excitation (given by the temperature-averaged excitation function α_{ji}) from the ground level (j) to the excited level (i), and that the ionization temperature is equal to the electron temperature. The quantities A_Z (abundance of element Z), a_{Zz} (population of ionization stage z of element Z), a_H (number of hydrogen atoms per electron), and the excitation functions are taken from Mewe and Gronenschild (55). Only the strongest lines in the bandpass, Fe IX (171 Å), Fe X (174.5 Å), O V (172.2 Å), O VI (173 Å), and Ne IV (172.6 Å), were included in the computation. The densities derived (Fig. 6) are in good agreement with earlier EUV and soft x-ray results (52–54) and with earlier eclipse results (56) for less than 1.4 solar radii, and extend the EUV analysis of plume structure to about 1.7 solar radii (57). The plumes near the edge of the polar coronal holes tilt outward toward lower latitudes as compared to the radial direction. The plume that is plotted in Fig. 6 is tilted about 20° away from the radial direction.

Future applications of normal-incidence x-ray optics. Our data demonstrate that normal-incidence multilayer x-ray telescopes can form high-resolution images with significantly lowered levels of x-ray scatter. Furthermore, these systems are not subject to acute optical aberration effects over reasonable fields of view. We anticipate that multilayer telescopes will provide solar x-ray images with spatial resolution approaching 0.1 arc second in the near future in well-defined spectral bands with excellent sensitivity. Additional capabilities that can be anticipated with multilayer optics, such as multilayer gratings, zone plates, and compound systems incorporating grazing-incidence primary mirrors and multilayer magnifying optics (27) or multilayer Rowland circle grating or “crystal” spectrometers (19) should extend the utility of multilayer optics to shorter wavelengths and provide astronomers with powerful high spectral

resolution instruments that are stigmatic. These instruments should allow the study of fundamental problems in solar physics such as (i) the structure, dynamics, and energy balance (including the heating source or sources) of coronal loops, (ii) the mechanism responsible for generating the solar wind, and (iii) the configurations in the corona which are necessary for the onset of flares.

The application of multilayer optics to nonsolar x-ray astronomy should prove extremely fruitful, as well. X-ray astronomy has revealed the existence of high-temperature astrophysical phenomena that range from thousands of kilometers to megaparsecs (58–60). Although not as bright from Earth as the sun, many cosmic x-ray sources have complex extended thermal and spatial structure. Among such sources are supernova remnants (61), the hot component of the interstellar medium in our galaxy (62) and in other nearby galaxies, and the hot intracluster gas bound in clusters of galaxies (60). The study of the thermal and density structure of these extended cosmic plasmas may be possible with the use of multilayer optics coupled to grazing-incidence optical primary mirrors such as the Advanced X-Ray Astrophysics Facility (63). In addition, spectrally resolved images of the halos (64) caused by interstellar scattering, which surround the image of every compact x-ray source, can be used to address fundamental questions concerning the composition and structure of the interstellar dust (65).

In summary, we have used normal-incidence multilayer optics to produce high spatial resolution full disk images of the sun in selected narrow wavebands in the soft x-ray–EUV. The photographic densities observed even in short exposures clearly reveal the high reflectivity and excellent waveband match of the primary and secondary multilayer mirrors in the Cassegrain telescope and also demonstrate the superiority of the new Eastman Kodak T-Grain emulsions over Schumann emulsions, which have long served as the photographic film of choice for soft x-ray–EUV observations (66). Multilayer optics can also lessen x-ray telescope system design requirements and yield improved image quality in an experimentally difficult spectral region. Multilayer optics do not exhibit the x-ray scattering characteristic of grazing-incidence telescopes. Consequently, small faint features can be clearly seen even though they are near bright loops or active regions. Because of these important technological developments, the images obtained during this flight have revealed features of the solar corona in greater detail at soft x-ray–EUV wavelengths. Clearly, multilayer optics will play a profound role in laboratory and astronomical x-ray imaging.

REFERENCES AND NOTES

1. J. Harvey, *Highlights Astron.* **4**, 223 (1977).
2. J. H. Underwood, J. E. Milligan, A. C. de Loach, R. B. Hoover, *Appl. Opt.* **16**, 858 (1977); G. S. Vaiana *et al.*, *Space Sci. Instrum.* **3**, 19 (1977).
3. P. Kirkpatrick and A. V. Bacz, *J. Opt. Soc. Am.* **38**, 766 (1948).
4. H. Wolter, *Ann. Phys.* **8**, 94 (1950); H. Wolter, *ibid.* **10**, 268 (1952).
5. R. Giacconi, W. P. Reidy, T. Zehnpfennig, J. C. Lindsay, W. S. Muney, *Astrophys. J.* **142**, 1274 (1965).
6. P. Gorenstein, B. Harris, H. Gursky, R. Giacconi, P. Vanden Bout, *Science* **172**, 369 (1971).
7. A. B. C. Walker, Jr., H. R. Rugge, K. Weiss, *Astrophys. J.* **188**, 423 (1988); *ibid.* **192**, 169 (1972); *ibid.* **194**, 471 (1974).
8. A. B. C. Walker, Jr., *Space Sci. Instrum.* **2**, 9 (1976).
9. T. W. Barbee, Jr., *Opt. Eng.* **25**, 898 (1986).
10. J. A. Trail, R. L. Byer, J. B. Kortright, in *X-Ray Microscopy II*, D. Sayer, Ed. (Springer-Verlag, Berlin, in press); E. Spiller, in *X-Ray Microscopy*, G. Schmahl and D. Rudolph, Eds. (Springer-Verlag, Berlin, 1984), pp. 226–231.
11. T. W. Barbee, Jr., P. Pianetta, R. Redaelli, R. Tatchyn, T. W. Barbee III, *Appl. Phys. Lett.* **50**, 1841 (1987).
12. J. F. Lindblom, A. B. C. Walker, Jr., T. W. Barbee, Jr., *Proc. Soc. Photo-Opt. Instrum. Eng.* **691**, 11 (1986).
13. L. Contardi, S. S. Chao, J. Keems, J. Tyler, *Scanning Electron Microscopy (Energy Conversion Devices, Inc., Troy, MI, 1984)*, part II, pp. 577–582.
14. D. K. Bowen, J. S. Elliott, S. R. Stock, S. D. Dover, *Proc. Soc. Photo-Opt. Instrum. Eng.* **691**, 94 (1986).
15. E. D. Franco and M. J. Boyle, *ibid.* **563**, 354 (1985).
16. The Skylab S-082A objective normal-incidence grating spectroheliograph [R.

- Tousey, J. D. F. Bartoe, G. E. Brueckner, J. D. Purcell, *Appl. Opt.* **16**, 870 (1977)] was able to provide spectroheliograms in solar lines at wavelengths as short as 170 Å. However, the low XUV efficiency of conventional optics limited S-082A non-flare observations at wavelengths shorter than 304 Å.
17. The Wolter type I telescope has an internally reflecting paraboloidal mirror followed by an internally reflecting coaxial and confocal hyperboloidal mirror.
 18. R. B. Hoover, R. J. Thomas, J. H. Underwood, *Adv. Space Sci. Tech.* **11**, 150ff (1972).
 19. J. A. R. Sampson, *Techniques of Vacuum Ultraviolet Spectroscopy* (Wiley, New York, 1967).
 20. E. Spiller, in *Low Energy X-Ray Diagnostics*, D. T. Attwood and B. L. Henke, Eds. (American Institute of Physics, 75th Conference Proceedings, New York, 1981), p. 124.
 21. T. W. Barbee, Jr., *ibid.*, p. 131.
 22. H. Brueggemann, *Conic Mirrors* (Focal Press, New York, 1968).
 23. J. H. Underwood and T. W. Barbee, Jr., *Nature* **294**, 429 (1981); J. P. Henry, E. Spiller, M. Weisskopf, *Appl. Phys. Lett.* **40**, 25 (1982); L. Golub, G. Nystrom, E. Spiller, J. Wilczynski, *Proc. Soc. Photo-Opt. Instrum. Eng.* **563**, 266 (1985).
 24. G. F. Marshall, Ed., *Proc. Soc. Photo-Opt. Instr. Eng.* **563** (1985); L. V. Knight and D. K. Bowen, Ed., *ibid.* **691** (1986).
 25. J. H. Underwood, M. E. Bruner, B. M. Haisch, W. A. Brown, L. W. Acton, *Science* **238**, 61 (1987).
 26. A. B. C. Walker, Jr., J. F. Lindblom, R. B. Hoover, T. W. Barbee, Jr., *J. Phys.-Colloque* **47** (1988).
 27. R. B. Hoover, D. L. Shealy, S. H. Chao, *Opt. Eng.* **25**, 970 (1986).
 28. The filters were manufactured by Luxel Corporation of Friday Harbor, WA.
 29. W. E. Behring, L. Cohen, U. Feldman, *Astrophys. J.* **175**, 493 (1972).
 30. M. Malinovsky and L. Heroux, *ibid.* **181**, 1009 (1973).
 31. G. A. Doschek and R. D. Cowan, *Astrophys. J. Suppl. Ser.* **56**, 67 (1984).
 32. D. L. Shealy, R. B. Hoover, D. Gabardi, *Proc. Soc. Photo-Opt. Instrum. Eng.* **691**, 83 (1986).
 33. T. W. Barbee, Jr., in *Synthetic Modulated Structures*, L. Chang and B. C. Giessen, Eds. (Academic Press, New York, 1985), pp. 313–337.
 34. T. W. Barbee, Jr., S. Mrowka, M. C. Hettrick, *Appl. Opt.* **24**, 883 (1985).
 35. J. A. Trail, R. L. Byer, T. W. Barbee, Jr., *Appl. Phys. Lett.*, in press.
 36. J. H. Underwood and T. W. Barbee, Jr., in *Low-Energy X-Ray Diagnostics*, D. T. Attwood and B. L. Henke, Eds. (American Institute of Physics, 75th Conference Proceedings, New York, 1981), p. 170.
 37. Manufactured by General Optics of Moorpark, CA.
 38. T. W. Barbee, Jr., unpublished data.
 39. J. E. Maskasky, *J. Imaging Sci.* **31**, 15 (1987).
 40. Examples of films with Schumann emulsions include the Kodak SWR, Kodak Pathé SC-5 and SC-7 and Kodak 101-07 and 104-07 films; V. Schumann, *Ann. Phys.* **5**, 349 (1901); R. Audren, *Appl. Opt.* **4**, 1596 (1966); M. E. Van Hoosier, J.-D. F. Bartoe, G. E. Brueckner, N. P. Patterson, R. Tousey, *ibid.* **16**, 887 (1977); A. G. Millikan and C. E. Coykendall, *Am. Astron. Soc. Photo. Bull.* **3**, 11 (1977).
 41. R. B. Hoover, T. W. Barbee, Jr., J. F. Lindblom, A. B. C. Walker, Jr., in *Kodak Technical Bits*, E. Eggleton, Ed. (Kodak, Rochester, summer 1988), p. 1.
 42. R. Giacconi, W. P. Reidy, G. S. Vaiana, L. P. Van Speybroeck, T. Zehnpfennig, *Space Sci. Rev.* **9**, 3 (1969).
 43. J. E. Vernazza and E. M. Reeves, *Astrophys. J. Suppl. Ser.* **37**, 485 (1978).
 44. G. Hass and W. R. Hunter, in *Space Optics*, B. J. Thompson and R. R. Shannon, Eds. (National Academy of Sciences, Washington, DC, 1974), pp. 525–553; U. Mayer, *Space Sci. Rev.* **3**, 781 (1964); S. M. Mrowka, P. Jelinsky, S. Bowyer, G. Sanger, W. J. Choyke, *Proc. Soc. Photo-Opt. Instrum. Eng.* **597**, 160 (1985); E. M. Reeves, M. C. H. Huber, J. G. Timothy, *Appl. Opt.* **16**, 837 (1977).
 45. G. L. Withbroe in *Solar Active Regions*, F. Q. Orrall, Ed. (Colorado Associated Univ. Press, Boulder, 1981), pp. 199–212.
 46. R. G. Athay, in *Physics of the Sun*, P. A. Sturrock, T. E. Holzer, D. M. Mimihalas, R. K. Ulrich, Eds. (Reidel, Dordrecht, 1985), vol. 2, pp. 51–70.
 47. G. L. Withbroe, in *Coronal Holes and High Speed Wind Streams*, J. B. Zirker, Ed. (Colorado Associated Univ. Press, Boulder, 1977), pp. 143–177.
 48. E. Tandberg-Hanssen, *Solar Prominences* (Reidel, Dordrecht, 1974).
 49. E. J. Schmahl and F. Q. Orrall, *Astrophys. J.* **231**, 241 (1979); E. J. Schmahl *et al.*, *Solar Phys.* **39**, 337 (1974).
 50. G. W. Pneuman and F. Q. Orrall, in *Physics of the Sun*, P. A. Sturrock, T. E. Holzer, D. M. Mimihalas, R. K. Ulrich, Eds. (Reidel, Dordrecht, 1986), vol. 2, pp. 71–134.
 51. G. L. Withbroe, in *Solar Flares and Coronal Physics Using P/OF As a Research Tool*, E. Tandberg-Hanssen, R. M. Wilson, H. S. Hudson, Eds. (NASA Conference Publication, NASA, Greenbelt, MD, **2421** 1986), pp. 221–240.
 52. I. A. Ahmad and G. L. Withbroe, *Solar Phys.* **53**, 397 (1977).
 53. J. D. Bohlin, N. R. Sheeley, R. Tousey, *Space Res.* **XV**, 651 (1978).
 54. I. A. Ahmad and D. F. Webb, *Solar Phys.* **58**, 323 (1978).
 55. R. Mewe and E. H. B. M Gronenschild, *Astron. Astrophys. Suppl. Ser.* **45**, 11 (1981).
 56. K. Saito, *Publ. Astron. Soc. Jpn.* **17** (1965).
 57. A more detailed analysis of these polar plume observations is in preparation.
 58. R. Giacconi, Ed., *X-Ray Astronomy with the Einstein Satellite* (Reidel, Dordrecht, 1981).
 59. R. Rosner, L. Golub, G. S. Vaiana, *Annu. Rev. Astron. Astrophys.* **23**, 413 (1985).
 60. W. Forman and C. Jones, *ibid.* **20**, 547 (1982).
 61. J. Danziger and P. Gorenstein, Eds., *Supernova Remnants and Their X-Ray Emission* (Reidel, Dordrecht, 1983).
 62. R. O. Williamson *et al.*, *Astrophys. J.* **193**, 133 (1974); L. L. Cowie and A. Sorguila, *Annu. Rev. Astron. Astrophys.* **24**, 499 (1986).
 63. M. C. Weisskopf, *Proc. Soc. Photo-Opt. Instrum. Eng.* **597**, 228 (1985).
 64. J. W. Overbeck, *Astrophys. J.* **141**, 864 (1965); R. C. Catura, *ibid.* **275**, 675 (1983).
 65. J. M. Greenberg, in *Cosmic Dust*, J. A. M. McDonnell, Ed. (Wiley, New York, 1978), pp. 187–294.
 66. R. B. Hoover, in preparation.
 67. We thank R. A. Van Patten, J. Gill, R. Hacker, J. Zerbe, J. Trail, M. Hettrick, J. C. Reily, D. Watson, J. McDougal, B. Hale, D. Javins, J. Smith, W. Bond, L. Mullaley, W. Bass, F. Rutledge, C. Kalange, D. R. Gabardi, D. L. Shealy, G. Steele, H. M. Cleare, K. Huff, G. Brown, A. DeWan, J. Pruss, R. Rakoff, H. Zimmer, C. Welch, J. Martinez, C. Martinez, F. Lau, and D. Patterson. We acknowledge useful discussion with R. Canfield and B. Labonte. This Project was funded by NASA grant NSG5131 and received its initial support through the Center Director's Discretionary Fund of NASA/MSFC. The data in Fig. 1C were obtained with the support of NASA grants NGL12-001-011 and NAG5-744.

13 July 1988; accepted 12 August 1988